Properties of the diffuse X-ray background in a high-resolution hydrodynamical simulation

M. Roncarelli,[1]★ L. Moscardini,[1]★ P. Tozzi,[2]★ S. Borgani,[3,4]★ L. M. Cheng,[5]★
A. Diaferio,[6]★ K. Dolag[7]★ and G. Murante[8]★

[1]*Dipartimento di Astronomia, Università di Bologna, via Ranzani 1, I-40127 Bologna, Italy*
[2]*INAF, Osservatorio Astronomico di Trieste, via Tiepolo 11, I-34131 Trieste, Italy*
[3]*Dipartimento di Astronomia, Università di Trieste, via Tiepolo 11, I-34131 Trieste, Italy*
[4]*INFN – National Institute for Nuclear Physics, Trieste, Italy*
[5]*Institute of Theoretical Physics, Chinese Academy of Sciences, Beijing 100080, China*
[6]*Dipartimento di Fisica Generale 'Amedeo Avogadro', Università di Torino, via Giuria 1, I-10125 Torino, Italy*
[7]*Max-Planck Institut fuer Astrophysik, Karl-Scwarzschild Strasse 1, D-85748 Garching, Germany*
[8]*INAF, Osservatorio Astronomico di Torino, Strada Osservatorio 20, I-10025 Pino Torinese, Italy*

ABSTRACT

We study the properties of the diffuse X-ray background by using the results of a cosmological hydrodynamical simulation of the concordance Λ cold dark matter (ΛCDM) model. The simulation follows gravitational and gas dynamics and includes a treatment of physical processes, such as radiative cooling, star formation and supernova feedback. From the simulation outputs, we produce a set of two-dimensional maps of the intergalactic medium X-ray emission integrated over redshift. We find that the signal in the soft (0.5–2 keV) band is lognormally distributed with a mean intensity of about 4×10^{-12} erg s^{-1} cm^{-2} deg^{-2}; approximately 40 per cent of the emission originates from warm-hot gas (defined as baryons with $10^5 < T < 10^7$ K), and 90 per cent comes from structures at $z < 0.9$. Since the spectrum is soft, being mostly provided by the intergalactic medium at low temperature, the total mean intensity in the hard (2–10 keV) X-ray band is smaller by a factor of about 4. In order to constrain the physical processes included in our simulation, we compare our results with the observed upper limit $(1.2 \pm 0.3) \times 10^{-12}$ erg s^{-1} cm^{-2} deg^{-2} of the soft X-ray emission due to diffuse gas. To this purpose, we remove the contributions of observable extended objects (groups and clusters of galaxies) from the simulated maps by adopting different detectability criteria which are calibrated on the properties of systems at intermediate redshifts observed by *Chandra*. We show that the simulated diffuse soft X-ray emission is consistent with the present observed upper limit. However, if future measurements will decrease the level of the unresolved X-ray background by a factor of 2, a more efficient feedback mechanism should be required to suppress the soft emission of the gas residing within filaments and group-size haloes.

Key words: hydrodynamics – galaxies: clusters: general – intergalactic medium – cosmology: theory – diffuse radiation – X-rays: general.

1 INTRODUCTION

A general result of hydrodynamic simulations of cosmic structure formation is that, during the formation of galaxy clusters via gravita-

★E-mail: mauro.roncarelli (MR); lauro.moscardini@unibo.it (LM); tozzi@ts.astro.it (PT); borgani@ts.astro.it (SB); clm@itp.ac.cn (LMC); diaferio@ph.unito.it (AD); kdolag@mpa-garching.mpg.de (KD); murante@to.astro.it (GM)

tional collapse, a large amount of gas remains out of these structures at the present time. An important fraction of the total baryons of the universe (roughly 40–50 per cent) undergoes a process of shock-heating that starts at $z \sim 2$ and heats the baryons to an intermediate temperature of 10^5–10^7 K: this gas phase is often referred to as the warm-hot intergalactic medium (WHIM) (see e.g. Croft et al. 2001; Davé et al. 2001). Simulations also show that these baryons are not uniformly distributed: they constitute a filamentary network linking the largest virialized objects, the so-called cosmic web (Bond, Kofman & Pogosyan 1996). The existence of these structures is

believed to be the solution to the missing baryon problem (see e.g. Cen & Ostriker 1999), namely the fact that more than half the normal matter is yet to be detected by instruments; in fact, the density of filaments is expected to be very low and consequently their detection is made difficult by both their extremely low surface brightness and projection effects (see, however, some first claimed detections in X-ray analyses; Zappacosta et al. 2002; Finoguenov, Briel & Henry 2003; Markevitch et al. 2003). In any case, the intermediate temperature of the cosmic web gas suggests that it can produce a non-negligible X-ray emission through thermal bremsstrahlung. Given the physical state of the gas, this emission is expected to appear mostly as a diffuse background at soft energies.

It is now generally accepted that some of the observed cluster X-ray properties, such as the scaling relations between mass, X-ray luminosity and temperature and their redshift evolution, the temperature profiles, or the entropy excess in the central regions of poor clusters and groups, cannot be reproduced by a simple model of gas dynamics based on gravitational heating alone (see the discussion in Rosati, Borgani & Norman 2002; Voit 2005, and references therein). In an attempt to explain these discrepancies, new processes have been included in the models of cluster formation, largely increasing the complexity of the physics of the intracluster medium (ICM): radiative cooling, energy feedback from supernovae (SNe) and active galactic nuclei (AGNs), thermal conduction, turbulence, magnetic fields, etc. (see e.g. Bower 1997; Cavaliere, Menci & Tozzi 1998; Balogh, Babul & Patton 1999; Bryan 2000; Pearce et al. 2000; Muanwong et al. 2001; Tozzi & Norman 2001; Voit & Bryan 2001b; Babul et al. 2002; Voit et al. 2002; Tornatore et al. 2003; Jubelgas, Springel & Dolag 2004; Di Matteo, Springel & Hernquist 2005; Dolag et al. 2005). All these processes affect the properties of both the gas within virialized objects, such as galaxy groups and clusters, and the diffuse gas component which has low density and temperature. Therefore, the expected X-ray emission from the cosmic web can sensitively change when the parameters describing the ICM physics are varied. For these reasons, observational data on the soft X-ray background (hereafter XRB) emitted by diffuse gas can be used as a probe of these physical processes, as suggested by different authors (see e.g. Bryan & Voit 2001; Voit & Bryan 2001a; Xue & Wu 2003).

Thanks to the latest generation of X-ray satellites (*Chandra* and *XMM–Newton*), the observational picture about the cosmic XRB in the soft (0.5–2 keV) energy band has become much clearer. Very deep pointed observations, such as the 1–2 Ms *Chandra* Deep Fields (CDFs) (Giacconi et al. 2002; Alexander et al. 2003) and the Lockman Hole *XMM–Newton* data (Worsley et al. 2004), showed that the soft XRB is largely produced by individual discrete sources, mostly AGNs. Recent estimates of the percentage of the resolved contribution range between 85 and 95 per cent (see e.g. Bauer et al. 2004; Worsley et al. 2005). These results give a conservative estimate of approximately $(1.2 \pm 0.3) \times 10^{-12}$ erg s^{-1} cm^{-2} deg^{-2} for the intensity of the still unresolved soft XRB (see the discussion in Section 6.1); therefore, this value can be used to set a stringent upper limit to the background from the diffuse intergalactic medium (IGM).

The availability of these new observational constraints suggests to reconsider the problem of the soft X-ray emission from the cosmic web and its implications for the ICM physics by updating an analysis made by Croft et al. (2001). The main goal of our paper is to check the consistency of our model with the observed limits by using the outputs of a cosmological hydrodynamic simulation (Borgani et al. 2004), which, besides gravitational and gas dynamics, includes a treatment of the ICM with radiative cooling, star formation and SN feedback. Our previous analyses (Borgani et al. 2004; Ettori et al.

2004; Diaferio et al. 2005) showed that the results of this simulation are in encouraging agreement with some of the most significant observed properties of clusters, such as the mass–temperature and the X-ray luminosity–temperature relations; however, the feedback mechanism does not appear to be efficient enough to avoid the production of overluminous groups and poor clusters.

The paper is organized as follows. In Section 2, we describe the characteristics of our simulation and present the procedure used to create the set of X-ray maps. The general statistical properties of the XRB extracted from these maps are discussed in Sections 3 and 4 for the soft (0.5–2 keV) and hard (2–10 keV) X-ray bands, respectively. Section 5 is devoted to the comparison of our results with previous works. In Section 6, we review the observational estimates of the contribution of diffuse gas to the soft XRB, and we compare them with the results of our mock maps in order to obtain qualitative constraints on the modelling of the physical processes included in our hydrodynamical simulation. We conclude in Section 7.

2 THE MAP CONSTRUCTION

2.1 The hydrodynamical simulation

The study of the properties of the diffuse X-ray emission from the large-scale structure of the universe and its comparison with observations requires the analysis of the total emission integrated over redshift. Therefore, we need to simulate the entire volume of the past light-cone seen by an observer located at $z = 0$. We construct the light-cone, which enables the production of simulated maps of the X-ray intensity, by using the outputs of a cosmological hydrodynamical simulation. Specifically, we use the results of the simulation by Borgani et al. (2004), which considers the concordance cosmological model, i.e. a flat Λ cold dark matter (ΛCDM) model dominated by the presence of the cosmological constant ($\Omega_{\mathrm{m}} = 0.3$, $\Omega_{\Lambda} = 0.7$), with a Hubble constant $H_0 = h \, 100 \, \mathrm{km \, s^{-1} \, Mpc^{-1}}$ and $h = 0.7$, and a baryon density $\Omega_{\mathrm{b}} = 0.04$. The initial conditions were set by the CDM power spectrum and were normalized by assuming $\sigma_8 = 0.8$. The run was carried out with the TREESPH code GADGET-2 (Springel, White & Hernquist 2001; Springel 2005) and followed the evolution of 480^3 dark matter (DM) particles and as many gas particles from $z = 49$ to $z = 0$. The cubic box is $192 \, h^{-1}$ Mpc on a side, and the DM and gas particles have mass $m_{\mathrm{DM}} = 4.62 \times 10^9 \, h^{-1} \, \mathrm{M_\odot}$ and $m_{\mathrm{gas}} = 6.93 \times 10^8 \, h^{-1} \, \mathrm{M_\odot}$, respectively. The Plummer-equivalent gravitational softening is $\epsilon = 7.5 \, h^{-1}$ kpc at $z = 0$, fixed in physical units between $z = 2$ and $z = 0$, and fixed in comoving units at earlier times.

The simulation, besides gravity and non-radiative hydrodynamics, includes a treatment of the processes that influence the physics of the ICM: star formation, by adopting a subresolution multiphase model for the interstellar medium (Springel & Hernquist 2003), feedback from SNe with the effect of weak galactic outflows, radiative gas cooling and heating by a uniform, time-dependent, photoionizing ultraviolet (UV) background. This run produced 100 outputs, equally spaced in the logarithm of the expansion factor, between $z = 9$ and $z = 0$.

2.2 The map-making procedure

In order to create mock maps of the X-ray emission of the structures within the past light-cone, we follow the same technique adopted by Croft et al. (2001) (see also similar applications for maps of the Sunyaev–Zel'dovich effect; e.g. da Silva et al. 2001; Springel, White & Hernquist 2001; White, Hernquist & Springel 2002). The

method is based on the replication of the original box volume along the line of sight. Since we assume a flat cosmological model, we use the comoving coordinates for the projection because the light trajectory is a straight line in this reference frame. We build past light-cones which extend to $z = 6$. Even if this maximum redshift can appear too large to still yield a significant signal in the X-ray band (this will be confirmed by our analysis in Section 3), this choice is done to obtain, at the same time, maps for the thermal and kinetic Sunyaev–Zel'dovich effects (not discussed in this paper), for which there is a non-negligible contribution from the high-redshift gas. The extension of the light-cone corresponds to a comoving distance of approximately $5770\,h^{-1}$ Mpc, so we need to stack the simulation volume roughly 30 times. However, in order to obtain a better redshift sampling, rather than stacking individual boxes, we adopt the following procedure. We divide the simulated box at each output redshift into three equal slices along the line of sight (each of them with a depth of $64\,h^{-1}$ Mpc); for the stacking procedure, we choose the slice extracted from the simulation output that better matches the redshift of the central point of the slice. Our light-cones are thus built with 91 slices extracted from 82 different snapshots.

The necessity of avoiding the repetition of the same structures along the line of sight requires a randomization of the boxes used to build our maps; since our simulation assumes periodic boundary conditions, for each box entering the light-cone, we combine a process of random recentring of the coordinates with a 50 per cent probability of reflecting each axis. The slices belonging to the same box undergo the same randomization process to avoid spatial discontinuities between them; this allows us to retain the entire information on the structures within the box and strongly reduces the loss of power on larger scales. By varying the initial random seeds, we also obtain different light-cone reconstructions; we use this technique to produce 10 different realizations that we use to assess the statistical robustness of our results.

In order to have maps covering a larger field of view, we replicate the boxes four times across the line of sight starting at comoving distances larger than half the light-cone extension (i.e. larger than about $2900\,h^{-1}$ Mpc, corresponding to $z > 1.4$). The strategy to pile up boxes is shown in Fig. 1. In this way, we obtain maps $3.78°$ on a side. Every map contains 8192 pixel on a side; consequently our resolution is 1.66 arcsec, roughly three times the resolution of the CDFs at the aim point.

We now need to calculate the contribution, to the X-ray emission, of every gas particle that lies within the light-cone volume. The X-ray luminosity of the ith particle in a given energy band $[E_1, E_2]$, as measured at $z = 0$, is calculated as

$$L_{X,i} = (\mu m_p)^{-2} x_e m_i \rho_i \Lambda(T_i, Z_i, E_1', E_2'), \tag{1}$$

where μ is the mean molecular weight in units of the proton mass m_p, x_e represents the ratio between the number density of free electrons and hydrogen nuclei (n_e/n_H), m_i and ρ_i are the particle mass and density, respectively. Since only the gas with $T > 10^5$ K gives a significant contribution to the X-ray emission, we can safely assume full ionization of hydrogen and helium for all the particles; therefore, the values of μ and x_e depend only on the metallicity (note that $\mu = 0.588$ and $x_e = 1.158$ for zero metallicity). The cooling function Λ is computed by using the plasma emission model by Raymond & Smith (1977) as a function of temperature T_i and metallicity Z_i of the particle and depends on the energy interval $[E_1', E_2']$; this interval is K-corrected for redshift: $E_{1,2}' = E_{1,2}(1 + z)$.

As we will discuss in the following section, a sizeable contribution to the soft XRB comes from relatively warm particles, with temperature below 10^7 K. At these temperatures, the emissivity from metal

Figure 1. Sketch of the configuration adopted to realize the light-cone. The observer is located at the position O at the centre of the lowest side of the first box. The past light-cone is obtained by stacking the comoving volumes of the simulation outputs at the corresponding redshift. In order to obtain a large field of view of size 3.78^2 deg^2, starting at $z = 1.4$, we use four replications of the box at the same redshift. The red lines show the volume in the light-cone corresponding to the field of view.

lines becomes non-negligible and, therefore, one needs to account for their contribution. In its original implementation, GADGET-2 includes a prescription to generate metals from SN explosions. This model assumes that only SN-II contributes to the chemical enrichment, under the assumption of instantaneous recycling, i.e. metals are released instantaneously when new stars form and the effect of stellar lifetimes is neglected (see e.g. Tornatore et al. 2004, for a more detailed implementation of chemical enrichment in GADGET-2). In equation (1), we adopt the value of metallicity Z_i yielded by this prescription to compute the luminosity of each gas particle.

We then calculate the contribution of the ith gas particle to the X-ray intensity $I_{X,i}$ as

$$I_{X,i} = L_{X,i} / \left[4\pi d_L(z)^2 A \right], \tag{2}$$

where $d_L(z)$ is the luminosity distance and A is the angular area covered by a pixel. This quantity is then distributed over the pixels by using a smoothed particle hydrodynamics (SPH) smoothing kernel given by

$$W(x) \propto \begin{cases} 1 - 6x^2 + 6x^3, & 0 \leqslant x < 0.5 \\ 2(1 - x)^3, & 0.5 < x \leqslant 1 \\ 0, & x > 1. \end{cases} \tag{3}$$

In the previous expressions, $x \equiv \Delta\theta/\alpha_i$, where $\Delta\theta$ is the angular distance between the pixel centre and the projected particle position and α_i is the angle subtended by the particle smoothing length provided by the hydrodynamical code. In order to conserve the total

intensity emitted by each particle, we normalize to unity the sum of the weights W over all 'touched' pixels. Finally, the intensity for a given pixel is obtained by summing over all the particles inside the light-cone.

To avoid spurious effects in the computation of the X-ray intensity, we exclude the particles having a mean electron density $n_e > 0.26 \, h^2 \, \mathrm{cm}^{-3}$. According to the model of Springel & Hernquist (2003), these particles are assumed to be composed by a hot ionized phase and a cold neutral phase, whose relative amounts depend on the local temperature and density. Since these particles are meant to account for the multiphase nature of the interstellar medium, we correctly exclude them from the computation of the X-ray emissivity.

3 THE PROPERTIES OF THE SOFT XRB

Examples of intensity maps obtained by adopting the method described above are displayed in Fig. 2 for the emission in the soft (0.5–2 keV) band. Following Croft et al. (2001), we distinguish two X-ray contributions: the contribution from the IGM (left-hand panel), i.e. from all the gas particles, and the contribution from the WHIM (right-hand panel), i.e. from the gas particles having a temperature between 10^5 and 10^7 K. The IGM map is dominated by several extended bright galaxy clusters (with flux in the range 10^{-12}–10^{-11} erg s^{-1} cm^{-2}) that give significant contributions to the total flux; there is also a large number of smaller structures, corresponding to nearby galaxy groups or distant fainter clusters. These smaller objects give the dominating contribution in the WHIM maps because the WHIM does not contain the hottest particles; on the contrary, in these maps, the brightest galaxy clusters are much less prominent. Note that, because of projection effects, neither maps show evident signatures of emission from filamentary structures.

The distribution of the values assumed by the intensity (considering the 1.66 arcsec pixel) is shown in Fig. 3 for both the IGM and the WHIM. The thin lines refer to each of the 10 light-cone realizations, while the thick solid line shows their average. A small dispersion between the different realization is evident: this is mainly due to the inclusion, in the maps, of a larger or smaller number of galaxy
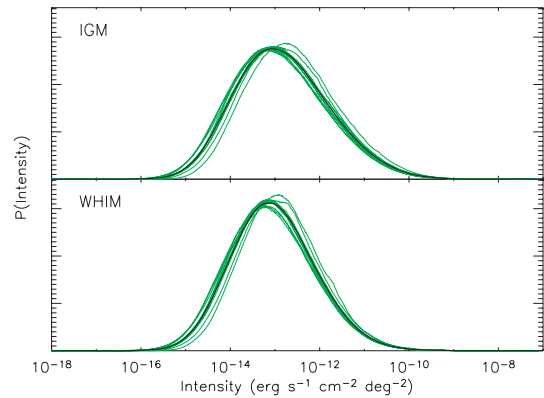

Figure 3. Distribution of pixel values of the intensity in the soft X-ray band. Upper and lower panels refer to the IGM and the WHIM, respectively. The thin lines show the results of 10 different realizations; the thick solid line is the corresponding average.

clusters at relatively low redshifts. In general, the two averaged distributions for $\mathcal{I} \equiv \log I_X$ (erg s^{-1} cm^{-2} deg^{-2}) are very close to the Gaussian distribution. In particular, we find $\overline{\mathcal{I}} = -12.81$ with a corresponding rms of 1.05 for the IGM, and $\overline{\mathcal{I}} = -13.01$ with a corresponding rms of 0.94 for the WHIM; the skewness is 0.30 and 0.25, for the IGM and the WHIM, respectively. Of course, the distributions differ for larger fluxes; this is due to the fact that the flux of the brightest structures comes from gas at high temperature.

The values of the intensity averaged over the 10 map realizations are reported in Table 1 for both the IGM and the WHIM. The quoted errors are the dispersions computed in fields of 1 deg^2 to allow a direct comparison with the corresponding results reported in Croft et al. (2001). We find that the mean intensity for the IGM is about 4×10^{-12} erg s^{-1} cm^{-2} deg^{-2}, a factor of 1.8 larger than that in Croft et al. (2001). The corresponding dispersion is also larger: about 50 per cent compared to about 20 per cent in Croft et al. (2001). Again, we checked that the high map-to-map spread is due to the presence of some bright galaxy clusters very close to the observer and giving a strong contribution to the total emission: this effect is
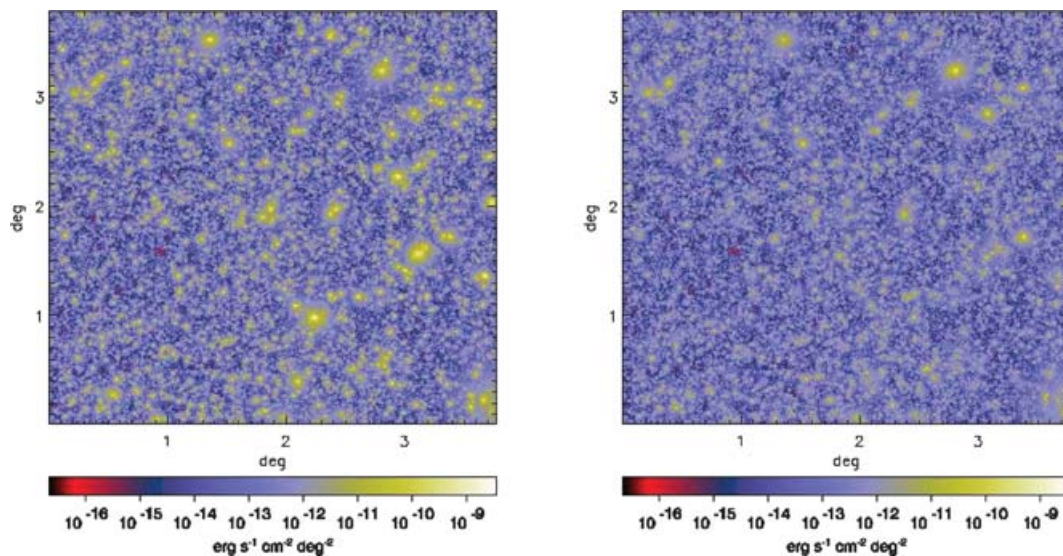

Figure 2. Maps of the soft (0.5–2 keV) X-ray intensity obtained by considering all the gas particles (IGM, left-hand panel), and only the gas particles with temperature in the range $10^5 < T < 10^7$ K (WHIM, right-hand panel). The maps are 3.78° on a side and the pixel size is (1.66 *arcsec*)^2. These two maps refer to the same realization of the past light-cone.

Table 1. Average value of the intensity I_X in the two different X-ray bands for the IGM and the WHIM. The average is computed over 10 different map realizations; the quoted errors are the rms in fields of 1 deg^2.

Energy band	IGM (total) (erg s^{-1} cm^{-2} deg^{-2})	WHIM (erg s^{-1} cm^{-2} deg^{-2})
Soft (0.5–2 keV)	$(4.06 \pm 2.19) \times 10^{-12}$	$(1.68 \pm 0.62) \times 10^{-12}$
Hard (2–10 keV)	$(1.01 \pm 1.53) \times 10^{-12}$	$(2.92 \pm 2.46) \times 10^{-14}$

also evident in the pixel distributions of individual maps shown in Fig. 3. By looking at the WHIM contribution, we find that its mean intensity is about 40 per cent of the total bremsstrahlung emission in the soft band (see Table 1). Again, this value is larger than in the analysis of Croft et al. (2001), who reported a value of 4.15×10^{-13} erg s^{-1} cm^{-2} deg^{-2}, corresponding to about 20 per cent of the total intensity of the IGM. However, we emphasize that we cannot make a direct comparison between these results and those presented in Croft et al. (2001) because the simulation analysed in that paper considers a much smaller box (50 h^{-1} Mpc on a side), assumes a slightly different cosmological model (a flat universe with $\Omega_m = 0.4$ and a primordial spectral index $n = 0.95$) and, most importantly, the included physical processes are not the same (see the discussion in Section 5).

To determine which sources contribute most to the soft X-ray emission, in Fig. 4 we show how the mean intensity varies when we include pixels with fluxes above a given threshold. The results show that the bremsstrahlung emission is dominated by very bright objects: pixels having a surface brightness larger than 10^{-10} erg s^{-1} cm^{-2} deg^{-2} (mainly corresponding to galaxy clusters and groups as shown in Section 6.2) contribute to more than 50 per cent of the total value, for both the IGM and the WHIM.

In order to have an indication of the typical distances of the soft X-ray sources, we follow Croft et al. (2001) and compute, for each pixel, the mean redshift of the particles contributing to the XRB weighted by their fluxes. The resulting map for the same IGM realization shown in the left-hand panel of Fig. 2 is displayed in Fig. 5 (left-hand panel). Almost all the bright clusters are at low redshift ($z < 0.15$), while the emission from the faintest structures mainly comes from redshifts around unity. This is confirmed by the distributions of the flux-weighted redshifts (central panel of Fig. 5), computed from the complete set of 10 realizations; the shapes of the distributions for the IGM and the WHIM are very similar, with a peak at $z \approx 0.7$. Note that few realizations have an excess of contri-
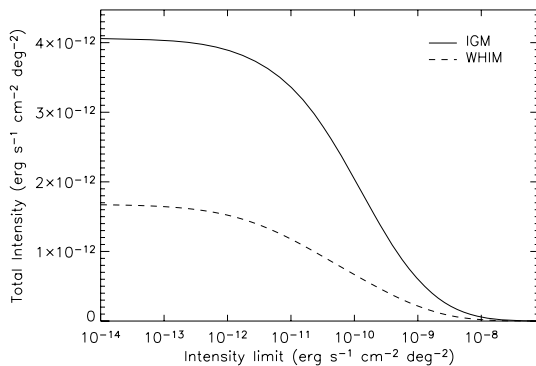

Figure 4. The value of the mean intensity (averaged over 10 different map realizations) as a function of the lower limit of the pixel surface brightness. The solid and dashed lines refer to the IGM and the WHIM, respectively.

bution from sources at relatively low redshift ($z < 0.15$): this is the origin of the large spread of the mean intensity previously discussed. The analysis of the maps also clearly shows how the projection of nearby and distant objects makes it very difficult to see imprints of the filamentary network present in the large-scale structure of the universe. Finally, in the right-hand panel of Fig. 5, we show the integrated soft X-ray intensity as a function of the limiting redshift. The curves for both the IGM and the WHIM reach half the total value at $z \simeq 0.3$, the 90 per cent level is reached around $z \simeq 0.9$ for the IGM and at $z \simeq 0.8$ for the WHIM. We can also note that the sources at $z > 2$ contribute less than 1 per cent of the soft X-ray flux.

3.1 The autocorrelation function

We analyse the clustering properties of the IGM in the soft X-ray band by estimating the autocorrelation function in our simulated maps. Following Croft et al. (2001), we calculate the contrast $\delta(\mathbf{x})$ defined as

$$\delta(\mathbf{x}) \equiv [I_X(\mathbf{x})/\overline{\mathcal{I}}] - 1, \tag{4}$$

where $I_X(\mathbf{x})$ is the surface brightness at the position $\mathbf{x}$ and $\overline{\mathcal{I}}$ is the average of each map. The contrast is then used to compute the angular correlation function as

$$w(\theta) = \langle \delta(\mathbf{x})\delta(\mathbf{x} + \boldsymbol{\theta}) \rangle. \tag{5}$$

The results are shown in Fig. 6, where we plot the average of the angular correlation functions calculated by considering the 10 different realizations of the light-cone; error bars are the error on the mean obtained from the scatter of the maps. We note that the mean function is always positive up to $\theta \sim 30$ arcmin, although some of the realizations show negative values for $\theta \gtrsim 8$ arcmin; the smallest scale at which $w(\theta)$ is compatible with a null value is 20 arcmin. From the plot, it is also evident a slow change of the logarithmic slope. This is confirmed by our analysis: by fitting our mean function under the assumption of a power-law relation, $w(\theta) \propto \theta^\alpha$, we find $\alpha \approx -0.9$ and $\alpha \approx -2.6$ in the intervals $0.1 < \theta < 2$ arcmin and $2 < \theta < 30$ arcmin, respectively.

Our results can directly be compared to those obtained by Croft et al. (2001). In general, the autocorrelation function extracted from our maps is larger by a factor of about 6. Moreover, we find that at large scales the decrease of their $w(\theta)$ is slower (they found $\alpha = -1.4$). These discrepancies can easily be explained by considering the differences between the two simulations. First, and most importantly, the size of the simulation box used by Croft et al. (2001) is about four times smaller than our box size; the resulting lack of large-scale power can lead to a significant underestimate of the clustering strength. Secondly, the physical processes included in our simulation produce higher values of the soft X-ray signal; as a consequence, the contrast δ also tends to be amplified, thus originating a larger autocorrelation function.

4 THE CONTRIBUTION IN THE HARD X-RAY BAND

It is well known that the hard (2–10 keV) X-ray band is strongly dominated by the emission from AGNs. However, a small portion of gas, mainly located within the richest clusters, is at high temperature and also gives some contribution in this band. The maps presented in Fig. 7 show the hard band intensity for the IGM and the WHIM (left- and right-hand panels, respectively), for the same light-cone
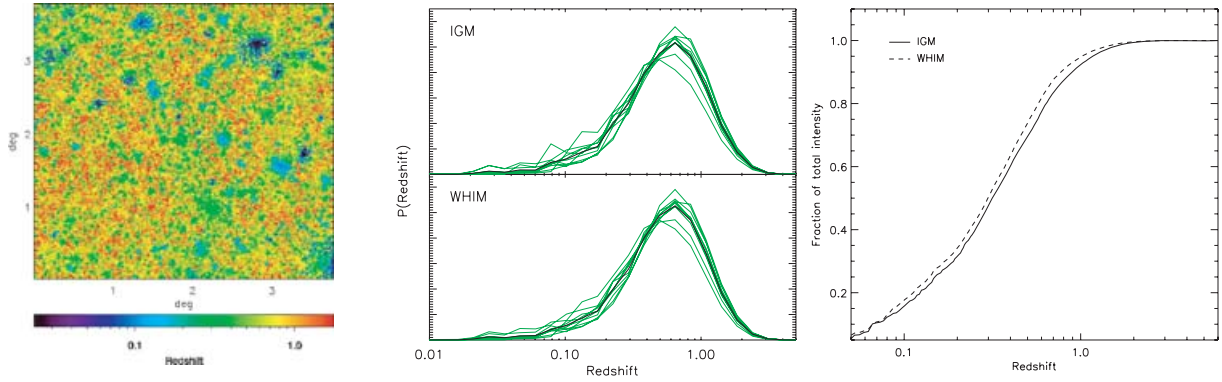
Figure 5. Left-hand panel: the map of the flux-weighted redshift, computed for the IGM in the soft X-ray band. The plot refers to the same light-cone realization shown in Fig. 2. Central panel: same as Fig. 3, but for the distribution of the flux-weighted redshift in the soft X-ray band. Right-hand panel: the integrated soft X-ray intensity (normalized to the total value) as a function of redshift. The solid and dashed lines refer to the IGM and the WHIM, respectively. The values plotted are the mean of 10 map realizations.

realization shown in Fig. 2. We note that, even if in some positions, corresponding to the hottest clusters, the intensity can reach values similar to those obtained in the soft X-ray maps (10^{-9} erg s^{-1} cm^{-2} deg^{-2}), outside virialized objects the hard X-ray maps are much fainter. In the map for the WHIM, the signal is strongly reduced and limited to the cluster atmospheres, with no evident emission from the diffuse gas; this makes the cosmic web not observable in this band because of its very low signal-to-noise ratio and projection effects. However, the high contrast between clusters and diffuse regions in the hard band maps suggests an empirical way to identify the positions of galaxy clusters in our simulated maps. This method will be used in Section 6 to separate the emission coming from extended objects from that produced by diffuse gas.

The small contribution of the IGM and the WHIM to the hard XRB is confirmed by the average total intensity reported in Table 1, for both components: we find about 1×10^{-12} erg s^{-1} cm^{-2} deg^{-2} and 3×10^{-14} erg s^{-1} cm^{-2} deg^{-2}, for the IGM and the WHIM, respectively. These values account for approximately 25 and 2 per cent of the corresponding mean intensity in the soft band. Note that, while for the WHIM our flux is a factor of 2 larger than Croft et al. (2001) result, for the IGM there is a substantial agreement. In fact, the lack of large-scale power in the simulation by Croft et al. (2001), due to the small box size, is compensated by the higher dynamical

evolution associated with the higher value of Ω_m, for a fixed power spectrum normalization σ_8 assumed in both analyses. Moreover, the effect of feedback on the hard X-ray emission by rich clusters is expected to be less relevant. We have to consider, however, that the field-to-field variance is quite large for the hard X-ray band because most of the signal comes from nearby bright clusters; in fact, the hard X-ray spectrum decreases exponentially and, even for hot objects, the bulk of the signal is rapidly shifted into the soft band at increasing redshifts.

A way to discriminate the AGN signal from that coming from clusters and the cosmic web is based on the energy flux hardness ratio (HR), here defined as the ratio between the intensities in the hard and soft bands at each pixel position: HR $\equiv I_X$[2–10 keV]$/I_X$[0.5–2 keV]. The emission from AGNs is in fact expected to have HR > 0.5, while much lower values are common for galaxy clusters and diffuse gas. The map for the HR obtained from the same IGM realization displayed in Figs 2 and 7 is shown in the left-hand panel of Fig. 8; in the plot it is easy to recognize the position of the richest galaxy clusters, while the connecting filamentary structure is almost completely absent. The distributions of the HR values for the 10 realizations and their average are shown in the right-hand panels, for both the IGM (up) and the WHIM (down). In the former case, the median value is around HR = 0.03, and less than a few per cent of the pixels have HR > 0.5; in the latter case, the median is smaller than 0.01 and no pixel has HR > 0.1.

5 COMPARISON WITH PREVIOUS WORKS

In this paper, we study the properties of the XRB from the large-scale structure of the universe. In particular, we followed the same method to build light-cone realizations applied by Croft et al. (2001), performing then similar statistical tests. From a comparison between our and their analysis, we found that in our soft X-ray maps the mean intensities of the IGM and the WHIM are larger than the intensities obtained by Croft et al. (2001) by a factor of 1.8 and 4, respectively. The autocorrelation function of the signal is also larger by a factor of about 6. As for the hard X-ray band, we find a substantial agreement with Croft et al. (2001) for the IGM contribution, while our contribution from the WHIM is a factor of 2 higher.

These differences can be understood in terms of the different characteristics of the two hydrodynamic simulations on which the analyses are based. The main reason for our higher values is that we followed the evolution of a much larger (almost 60 times) volume.
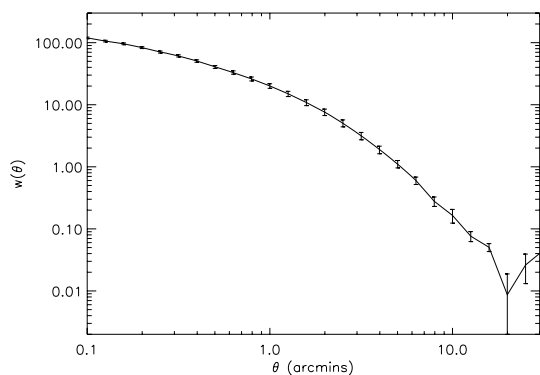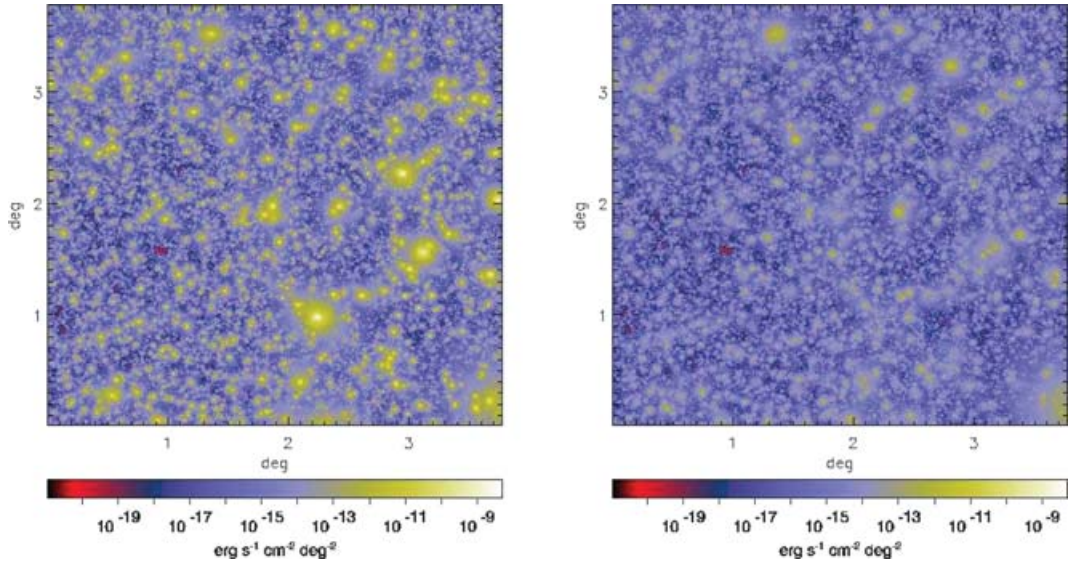

Figure 6. The angular correlation function of the IGM in the soft (0.5–2 keV) X-ray band. The solid line is the average over 10 different maps $3.78°$ on a side; error bars are the error on the mean calculated from the scatter of the maps.

Figure 7. Maps of the hard (2–10 keV) X-ray intensity for the IGM and the WHIM (left- and right-hand panels, respectively). The map is 3.78° on a side and the pixel is 1.66 arcsec on a side. These maps have been obtained from the same light-cone realization shown in Fig. 2.

This allows us to obtain a better representation of very massive clusters that contribute to most of the emission (see the discussion in Section 3). The larger sampled volume is also the main motivation of our higher autocorrelation function, which includes the contribution of longer wavelength modes.

However, an important difference between the two hydrodynamic simulations is also related to the treatment of the physical processes affecting the evolution of the baryonic component. The simulation of Croft et al. (2001) did not consider the possible multiphase nature of the star-forming gas. For this reason, they had to resort a posteriori to a correction of their results to account for it. On the contrary, the GADGET-2 code used for our simulation follows the different physical processes (radiative cooling, star formation and SN feedback) in a self-consistent way. In particular, the inclusion of a phenomenological description of galactic winds provides a much more efficient energy feedback than that implemented in the simulation by Croft et al. (2001). Moreover, the code directly considers

the effect of a photoionizing time-dependent UV background. Globally, this gas treatment produces a larger fraction of WHIM. This explains why larger differences are found for the contributions of the WHIM, while less significant differences are found between the signals in the hard X-ray band, which are mostly originated by the hottest objects. We also assumed a cosmological model which is closer to that suggested by the most recent observational data with $\Omega_m = 0.3$, while Croft et al. (2001) adopted $\Omega_m = 0.4$; thus, we have a higher contribution from baryons at high redshifts due to the slower dynamical evolution of the structures. The apparent agreement of our result for the hard band emission of the IGM with Croft et al. (2001) is due to a combination of all of these factors (see the discussion in Section 4).

Finally, a similar result to the one of Croft et al. (2001) has been obtained also by Bryan & Voit (2001) for the soft X-ray emission of the IGM from their Adaptive Mesh Refinement (AMR) simulation which includes a simple feedback model. Again the difference with
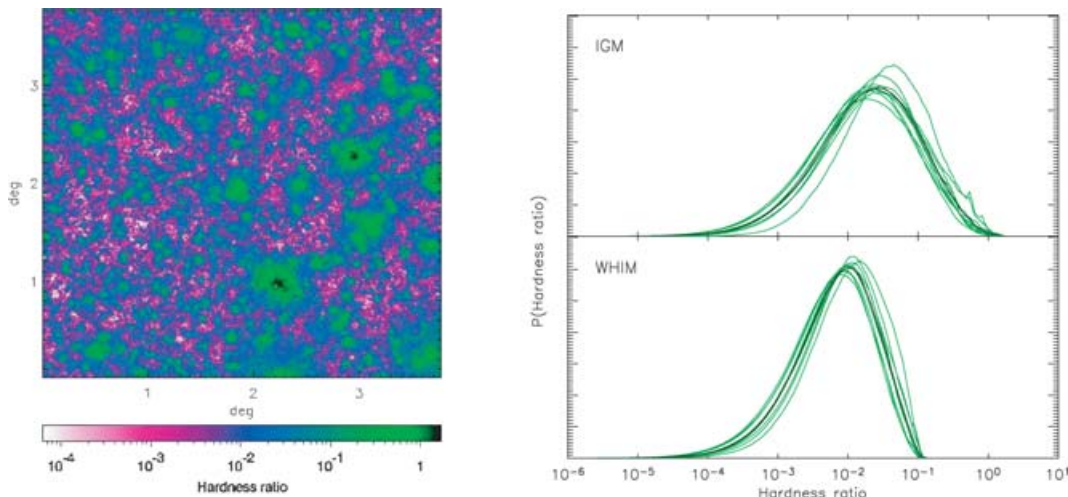

Figure 8. Left-hand panel: the map of the HR (hard band to soft band). This map is obtained from the same realization of the IGM light-cone shown in the left-hand panels of Figs 2 and 7. Right-hand panels: distribution of HR for the IGM (up) and for the WHIM (down). The thin lines show the results for 10 different realizations; the thick solid line is the corresponding average.

respect to the present work is mainly due to the relatively small volume sampled by their simulation.

6 THE CONTRIBUTION OF DIFFUSE GAS TO THE SOFT XRB

The goal of this section is to extract, from the soft X-ray maps discussed above, the contribution produced by the cosmic web, i.e. the baryons which are not included in the groups and clusters of galaxies currently identified in deep X-ray surveys. In order to check whether the modelling of the physical processes treated by our hydrodynamical simulation (which also influence the low-density gas regions) is reliable, we compare our results with observational estimates (mainly upper limits). We have to note that in the literature, as reviewed in the following subsection, there is no robust determination of the contribution of diffuse gas to the soft XRB; the value that we will use later for comparison is based, to some extent, on interpretation of the existing data.

6.1 Observational estimates

In recent years, thanks to the availability of new X-ray satellites like *Chandra* and *XMM–Newton*, there have been many efforts to measure the total XRB and to resolve it in its different components (see e.g. Giacconi et al. 2002; Moretti et al. 2002; Alexander et al. 2003; Bauer et al. 2004; Worsley et al. 2004, and references therein). In fact, the possibility of recognizing the discrete sources which give the main contribution opens new windows to study the connection between AGNs and galaxy formation and, most importantly for this work, constrains the possible signals from the diffuse gas.

At present, the most reliable estimate of the total XRB in the soft (0.5–2 keV) band has been obtained by Worsley et al. (2005). By assuming the shape of the XRB in the (1–8 keV) band determined by De Luca & Molendi (2004) from *BeppoSAX* data, and by taking into account the steepening of the spectrum below 1 keV as found by Roberts & Warwick (2001), Worsley et al. (2005) estimate an XRB $(0.5\text{--}2\,\text{keV}) = (8.12 \pm 0.23) \times 10^{-12}\,\text{erg s}^{-1}\,\text{cm}^{-2}\,\text{deg}^{-2}$. Note that this value is larger than the one adopted by Bauer et al. (2004), who found XRB $(0.5\text{--}2\,\text{keV}) = (7.52 \pm 0.35) \times 10^{-12}\,\text{erg s}^{-1}\,\text{cm}^{-2}\,\text{deg}^{-2}$. The discrepancy is originated by the fact that Bauer et al. (2004) extrapolate the hard spectrum in the soft band by assuming a slope of -1.4; of course, this does not take into account the steepening due to the non-AGN contribution, which, by the way, is the one we are most interested in. This total value includes any contribution, namely the Local Hot Bubble, the Galactic halo, unresolved galactic stars, and most importantly, the extragalactic components (both bright and faint) from point sources (AGNs), clusters, groups and the truly diffuse gas. The resolved (to date) XRB in the soft band produced by these extragalactic sources has been recently estimated by Worsley et al. (2005), who found $(6.9 \pm 0.2) \times 10^{-12}\,\text{erg s}^{-1}\,\text{cm}^{-2}\,\text{deg}^{-2}$. Similar results for the resolved component are presented by Bauer et al. (2004): $(6.7 \pm 0.3) \times 10^{-12}\,\text{erg s}^{-1}\,\text{cm}^{-2}\,\text{deg}^{-2}$. Therefore, by assuming the values found by Worsley et al. (2005) for the total XRB in the soft band, the emission which is still unresolved is approximately $(1.2 \pm 0.3) \times 10^{-12}\,\text{erg s}^{-1}\,\text{cm}^{-2}\,\text{deg}^{-2}$. This value represents an upper limit to the possible contribution from the diffuse gas because it still includes the unknown Galactic and Local Hot Bubble contributions. Note that the latter components probably dominate the XRB below 0.5 keV, making highly uncertain the estimate of the extragalactic contribution in the lowest X-ray energy band, where the signal from the cosmic web is expected to be even more significant.

6.2 Separating the diffuse soft X-ray emission from galaxy groups and clusters in the simulated maps

By comparing naively the estimates of the IGM soft X-ray contribution reported in Table 1 with the observational data discussed above, we would note that our simulated XRB accounts for about 50 per cent of the observed value of the XRB, but it is much larger (by a factor of 4) than the observed upper limit obtained by removing the discrete sources. Even considering the signal from the WHIM only, i.e. from gas having temperature between 10^5 and 10^7 K, the signal in our maps would be too large. However, this comparison is quite misleading because in the results from the simulation we still include the portion of the warm gas located in groups or in the external atmospheres of galaxy clusters; on the contrary, this gas is not present in the observed value $1.2 \pm 0.3 \times 10^{-12}\,\text{erg s}^{-1}\,\text{cm}^{-2}\,\text{deg}^{-2}$. For this reason, we need a more detailed analysis of our maps, where these objects need to be excluded.

We already know, from the previous analysis of our original hydrodynamical simulation (see e.g. Borgani et al. 2004), that the modelling of the included physical processes produces overluminous groups and poor clusters of galaxies. As discussed in that paper, additional sources of energy (such as feedback from SN-Ia or AGNs) would help to solve this discrepancy. This excess is located in high-density regions, whereas we are interested in the soft X-ray emission from the cosmic web; therefore, we need to identify and remove the X-ray extended sources, which correspond to galaxy clusters and groups, from the total intensity of our maps.

The proper procedure would be to identify and remove all the clusters and groups from mock observations of our simulated volumes. In practice, this is unfeasible because it would require simulating a full wide-area survey with all the related observational aspects, which is far beyond the aim of this paper. Therefore, we will remove clusters and groups on the basis of their total flux as it appears on our flux maps. To establish a definition of a cluster or a group to be applied to our bidimensional maps, we use an identification criterion based on the surface brightness value. We identify as an X-ray extended source (group or cluster) all the connected regions of pixel above a surface brightness threshold.

To accomplish this, we use the maps in the hard (2–10 keV) band because the emission from the diffuse gas in this band is much lower than in the soft band and therefore it is easier to identify the regions corresponding to virialized haloes (see Fig. 7). Then, we choose the value of the surface brightness threshold by inspecting the faintest groups identified in the deepest X-ray observations to date. Specifically, we consider a group (CDFS-594) identified in the CDF South (Giacconi et al. 2002) at $z \sim 0.7\text{--}0.8$. Its emission is detected with a high signal-to-noise ratio over a circular region of approximately 2700 arcsec^2. After fitting its spectrum with a *mekal* model (see e.g. Liedahl, Osterheld & Goldstein 1995, and references therein), we obtain a temperature of about 2.1 keV. Therefore, the corresponding *average* surface brightness in the hard band is $3.06 \times 10^{-12}\,\text{erg s}^{-1}\,\text{cm}^{-2}\,\text{deg}^{-2}$, which will be used as the reference value in the following analysis.[1] Note that this average value corresponds to the central part of the group (typically about three core radii), which is the region where the emission can realistically be detected. However, some emission associated with the X-ray halo is expected to provide subthreshold contribution up to the virial radius. Since we want to remove all the X-ray emission associated with a given halo,

---

[1] Similar results are obtained by considering a different galaxy group (CDFS-645), again identified in the CDF South exposure.

in the following analysis we will also consider smaller, up to eight times, surface brightness thresholds. We choose these thresholds because the surface brightness of an isothermal gas in the central region (about three core radii) is roughly eight times larger than at the virial radius. Finally, we consider a threshold for the minimum angular size of the region that can be identified as a group or a cluster. For this purpose, we choose a reference physical length of 100 kpc, that corresponds to a minimum angular size of $\sim$10 arcsec (at $z \sim 1$) for the cosmological model assumed in our simulation; this gives a minimum angular surface of $\sim$310 arcsec^2. This quantity roughly corresponds to the minimum size of the central detectable regions of X-ray groups (see Willis et al. 2005). This last criterion has a small impact on the final results (i.e. the expected average surface brightness of the cosmic web changes of few per cent when doubling the minimum angular size of the haloes).

6.3 The soft X-ray emission from the cosmic web in the simulated maps

By applying the previously discussed thresholds of the surface brightness and size on the maps produced in the hard (2–10 keV) X-ray band, we create a catalogue of connected regions corresponding to the extended objects such as groups and clusters. We use them as a mask on the soft (0.5–2 keV) X-ray maps to remove their emission and finally obtain the diffuse contribution. By averaging over our 10 different realizations, we find that the signal from the diffuse gas is 1.57×10^{-12} erg s^{-1} cm^{-2} deg^{-2} which is comparable to the observed upper limit. 69 per cent of the diffuse emission comes from gas with temperature in the range 10^5–10^7 K, whereas the total contribution of clusters and groups to the XRB is 2.49×10^{-12} erg s^{-1} cm^{-2} deg^{-2}; this value is larger than the total contribution from clusters and groups estimated from the observed number counts (Rosati et al. 2002; see also the corresponding discussion at the end of this section). As noted above, the adopted surface brightness threshold can be considered as an average of the group emission at intermediate redshifts, and then it could be too high to account for all clusters' and groups' emission. In fact, we find that 31 per cent of the 1.57×10^{-12} erg s^{-1} cm^{-2} deg^{-2} emission is still produced by gas having a temperature larger than 10^7 K. This is further confirmed by a visual inspection of the masked maps: the external regions of nearby clusters are not excluded. This is an indication that in general the surface brightness threshold defining high-density regions associated with groups and clusters of galaxies is probably lower than the adopted value. For this reason, we repeat the previous analysis
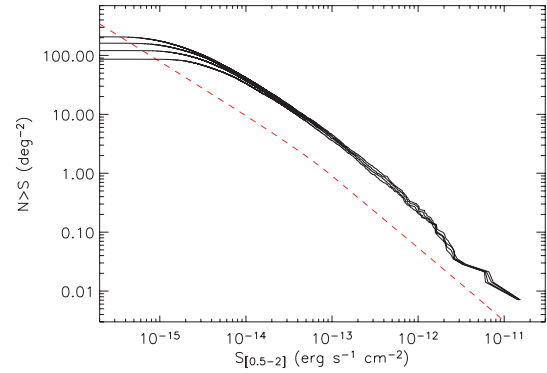

Figure 9. Number of objects as a function of the limiting flux in the soft (0.5–2 keV) X-ray band. The black solid lines are the results obtained by considering the connected regions with four different surface brightness cuts (see Table 2, for the adopted values). For comparison, we show (red dashed line) the observational data obtained by Rosati et al. (2002) by combining the results from the *ROSAT* Deep Cluster Survey (Rosati et al. 1998), EMSS (Rosati et al. 1995), BCS (Ebeling et al. 1998) and REFLEX (Boehringer et al. 2001).

by using thresholds which are smaller by a factor of 2, 4 and 8. The results, reported in Table 2, show a reduction of the contribution of the diffuse gas by a factor of 2 when the surface brightness cut is eight times smaller; the corresponding fraction of the signal from the WHIM increases up to 82 per cent. In general, we can conclude that the soft X-ray emission from the diffuse gas computed from our simulation is consistent with the upper limit coming from observational data. The feedback model we are assuming is efficient in the WHIM and/or in regions with intermediate density, although it can show problems in the deepest potential wells.

Finally, as a self-consistency check, we compute the $\log N - \log S$ function (always in the soft X-ray band) for our connected regions. The results are shown in Fig. 9 for the four different thresholds reported in Table 2. Again, we note the excess with respect to the observational data, represented by a combination of data made by Rosati et al. (2002) and coming from the *ROSAT* Deep Cluster Survey (Rosati et al. 1998), *Einstein* Medium Sensitivity Survey (EMSS) (Rosati et al. 1995), BCS (Brightest Cluster Sample; Ebeling et al. 1998) and REFLEX (*ROSAT*–ESO Flux-Limited X-Ray; Boehringer et al. 2001). This excess is produced by the overluminous objects which are present in our simulation at all relevant redshifts; for this reason, number counts are overestimated over the

Table 2. Contribution to the soft (0.5–2 keV) XRB of galaxy clusters and groups (Column 2) and of the diffuse gas (Column 3) as a function of the adopted threshold of the surface brightness (Column 1). We also report the percentage of the diffuse contribution coming from the WHIM (Column 4). The quoted errors are the rms in fields of 1 deg^2. All values are in units of 10^{-12} erg s^{-1} cm^{-2} deg^{-2}.

Surface brightness threshold in the hard (2–10 keV) X-ray band	Soft (0.5–2 keV) XRB (10^{-12} erg s^{-1} cm^{-2} deg^{-2})		
	Contributions from		
	Clusters and groups	Diffuse gas	Per cent WHIM
3.06	2.49 ± 2.04	1.57 ± 0.27	69 ± 13
1.53	2.78 ± 2.10	1.28 ± 0.19	73 ± 12
0.77	3.05 ± 2.14	1.01 ± 0.13	78 ± 11
0.38	3.28 ± 2.17	0.78 ± 0.09	82 ± 11
Observational upper limit		1.2 ± 0.3	

entire flux range. Finally, the apparent flattening at low fluxes ($S \approx 10^{-15}$ erg s^{-1} cm^{-2}) is originated by both resolution effects and the surface brightness limit assumed for the identification of the extended sources.

7 CONCLUSIONS

In this paper, we have used a cosmological hydrodynamical simulation of a concordance ΛCDM model to discuss the properties of the diffuse XRB. The simulation (Borgani et al. 2004) includes many relevant physical processes affecting the gas component. Indeed, the numerical treatment accounts for a time-dependent, photoionizing UV uniform background, radiative cooling processes within an optically thin gas of hydrogen and helium in collisional ionization equilibrium, star formation events and feedback processes from both SN-II and galactic winds. Our previous analyses (Borgani et al. 2004; Ettori et al. 2004) showed that the results of this simulation are consistent with several observational X-ray properties of galaxy clusters. However, there is also a number of discrepancies that remain unaccounted for; in particular, the cluster X-ray luminosity–temperature relation extracted from our simulation appears too high, i.e. there are overluminous groups and small clusters.

As suggested by different authors (see e.g. Bryan & Voit 2001; Voit & Bryan 2001a; Xue & Wu 2003), an alternative way to constrain the model describing the thermal properties of baryons and their cosmic history is related to the soft X-ray emission from diffuse gas. Indeed, a model of heating and cooling of the IGM makes predictions in terms of diffuse emission from filaments and unresolved structures. These predictions can be compared with the observational measurements of the XRB, which are now available (in the form of upper limits), thanks to the deep *Chandra* data.

In order to test the model included in our simulation, we follow the method of Croft et al. (2001) and, starting from the simulation snapshots, we constructed a set of 10 different two-dimensional maps, of size $(3.78°)^2$, of the past light-cone back to $z = 6$. The present analysis extends the previous work of Croft et al. (2001), thanks to a much larger volume sampling, to a more realistic representation of the physical processes affecting the baryon history and to the comparison with the observed XRB data after the *Chandra* era.

The main results obtained by using our set of maps are as follows.

(i) The mean intensity of the IGM in the soft (0.5–2 keV) X-ray band is about 4.1×10^{-12} erg s^{-1} cm^{-2} deg^{-2}; when considering the WHIM (defined as gas with temperature between 10^5 and 10^7 K), the mean intensity reduces to about 1.7×10^{-12} erg s^{-1} cm^{-2} deg^{-2}. The distribution of the intensity in the maps is very similar to a lognormal. 90 per cent of the signal comes from structures at $z \lesssim 0.9$.

(ii) As expected, in the hard (2–10 keV) X-ray band the total mean intensity is smaller (by a factor of 4) than in the soft one and becomes almost negligible when considering the WHIM (about 3×10^{-14} erg s^{-1} cm^{-2} deg^{-2}). The HR in the maps has a distribution which peaks at low values, with a median close to 0.03, which enables an easy discrimination of the AGN signal.

(iii) We obtain an estimate of $(0.8–1.6) \times 10^{-12}$ erg s^{-1} cm^{-2} deg^{-2} for the soft X-ray emission from the diffuse gas after removing the regions corresponding to extended objects, such as galaxy groups and clusters, from the maps. Our result is consistent with the present upper limit coming from observational data: $(1.2 \pm 0.3) \times 10^{-12}$ erg s^{-1} cm^{-2} deg^{-2}. This value, recently obtained by Worsley et al. (2005), has been estimated by removing the contri-

bution of resolved sources (AGNs, groups and clusters of galaxies) from the total XRB.

As a conclusion, our results show that the physical processes discussed here are consistent with existing constraints on the X-ray properties of the warm-hot baryons. However, if in the near future the measurements of the possible contribution from Galactic and local structures (still included in the observational upper limits) will reduce the maximum allowed emission from the diffuse gas by a factor of 2 or more, our predictions will start to conflict with the data. In this case, it will be required a more efficient mechanism of feedback acting on the gas with intermediate temperatures and densities; in fact, the presence of a stronger feedback would place the gas on a higher adiabat, thereby preventing it from reaching high densities and, on turn, suppressing the diffuse emission.

Our analysis confirms that the comparison between observational constraints on the diffuse emission in the soft X-ray band and results from cosmological hydrodynamical simulations enables us to gain information on the thermodynamical history of the diffuse baryons. In the future, it will be interesting to study some detailed simulated observations of the diffuse gas to check its detectability not only through bremsstrahlung emission, but also via emission and/or absorption of oxygen lines (O VI, O VII and O VIII); real observations will probably be provided by some dedicated wide-field high-resolution spectroscopic experiments now in project. It will also be relevant to compare simulated results with observations performed by the next generation of X-ray spectroscopic satellites, like *Constellation-X/XEUS* or *NeXT*, provided that their field of view is large enough to cover the filamentary structure of the cosmic web.

REFERENCES

Alexander D. M. et al., 2003, AJ, 126, 539
Babul A., Balogh M. L., Lewis G. F., Poole G. B., 2002, MNRAS, 330, 329
Balogh M. L., Babul A., Patton D. R., 1999, MNRAS, 307, 463
Bauer F. E., Alexander D. M., Brandt W. N., Schneider D. P., Treister E., Hornschemeier A. E., Garmire G. P., 2004, AJ, 128, 2048
Boehringer H. et al., 2001, A&A, 369, 826
Bond J. R., Kofman L., Pogosyan D., 1996, Nat, 380, 603
Borgani S. et al., 2004, MNRAS, 348, 1078
Bower R. G., 1997, MNRAS, 288, 355
Bryan G. L., 2000, ApJ, 544, L1
Bryan G. L., Voit G. M., 2001, ApJ, 556, 590
Cavaliere A., Menci N., Tozzi P., 1998, ApJ, 501, 493
Cen R., Ostriker J. P., 1999, ApJ, 514, 1
Croft R. A. C., Di Matteo T., Davé R., Hernquist L., Katz N., Fardal M. A., Weinberg D. H., 2001, ApJ, 557, 67
da Silva A. C., Kay S. T., Liddle A. R., Thomas P. A., Pearce F. R., Barbosa D., 2001, ApJ, 561, L15
Davé R. et al., 2001, ApJ, 552, 473

De Luca A., Molendi S., 2004, A&A, 419, 837

Diaferio A. et al., 2005, MNRAS, 356, 1477

Di Matteo T., Springel V., Hernquist L., 2005, Nat, 433, 604

Dolag K., Grasso D., Springel V., Tkachev I., 2005, J. Cosmol. Astropart. Phys., 1, 9

Ebeling H., Edge A. C., Bohringer H., Allen S. W., Crawford C. S., Fabian A. C., Voges W., Huchra J. P., 1998, MNRAS, 301, 881

Ettori S. et al., 2004, MNRAS, 354, 111

Finoguenov A., Briel U. G., Henry J. P., 2003, A&A, 410, 777

Giacconi R. et al., 2002, ApJS, 139, 369

Jubelgas M., Springel V., Dolag K., 2004, MNRAS, 351, 423

Liedahl D. A., Osterheld A. L., Goldstein W. H., 1995, ApJ, 438, L115

Markevitch M. et al., 2003, ApJ, 583, 70

Moretti A., Lazzati D., Campana S., Tagliaferri G., 2002, ApJ, 570, 502

Muanwong O., Thomas P. A., Kay S. T., Pearce F. R., Couchman H. M. P., 2001, ApJ, 552, L27

Pearce F. R., Thomas P. A., Couchman H. M. P., Edge A. C., 2000, MNRAS, 317, 1029

Raymond J. C., Smith B. W., 1977, ApJS, 35, 419

Roberts T. P., Warwick R. S., 2001, in Giacconi R., Serio S., Stella L., eds, ASP Conf. Ser., Vol. 234, X-Ray Astronomy 2000. Astron. Soc. Pac., San Francisco, p. 569

Rosati P., della Ceca R., Burg R., Norman C., Giacconi R., 1995, ApJ, 445, L11

Rosati P., della Ceca R., Norman C., Giacconi R., 1998, ApJ, 492, L21

Rosati P., Borgani S., Norman C., 2002, ARA&A, 40, 539

Springel V., 2005, MNRAS, 364, 1105

Springel V., Hernquist L., 2003, MNRAS, 339, 289

Springel V., White M., Hernquist L., 2001, ApJ, 549, 681

Tornatore L., Borgani S., Springel V., Matteucci F., Menci N., Murante G., 2003, MNRAS, 342, 1025

Tornatore L., Borgani S., Matteucci F., Recchi S., Tozzi P., 2004, MNRAS, 349, L19

Tozzi P., Norman C., 2001, ApJ, 546, 63

Voit G. M., 2005, Rev. Mod. Phys., 77, 207

Voit G. M., Bryan G. L., 2001a, ApJ, 551, L139

Voit G. M., Bryan G. L., 2001b, Nat, 414, 425

Voit G. M., Bryan G. L., Balogh M. L., Bower R. G., 2002, ApJ, 576, 601

White M., Hernquist L., Springel V., 2002, ApJ, 579, 16

Willis J. P. et al., 2005, MNRAS, 363, 675

Worsley M. A., Fabian A. C., Barcons X., Mateos S., Hasinger G., Brunner H., 2004, MNRAS, 352, L28

Worsley M. A. et al., 2005, MNRAS, 357, 1281

Xue Y., Wu X., 2003, ApJ, 584, 34

Zappacosta L., Mannucci F., Maiolino R., Gilli R., Ferrara A., Finoguenov A., Nagar N. M., Axon D. J., 2002, A&A, 394, 7

This paper has been typeset from a TeX/LaTeX file prepared by the author.